

Dual-Polarization Second-Order Photonic Topological Insulators

Yafeng Chen,^{1,2,§} Fei Meng,^{3,§} Zhihao Lan,^{4,*} Baohua Jia,^{3,†} and Xiaodong Huang^{3,‡}

¹*Key Laboratory of Advanced Technology for Vehicle Body Design and Manufacture, Hunan University, Changsha, 410082, China*

²*Department of Mechanical Engineering, Hong Kong Polytechnic University, Hong Kong SAR, China*

³*Faculty of Science, Engineering and Technology, Swinburne University of Technology, Hawthorn, Victoria 3122, Australia*

⁴*Department of Electronic and Electrical Engineering, University College London, Torrington Place, London WC1E 7JE, United Kingdom*



(Received 2 December 2020; revised 5 February 2021; accepted 23 February 2021; published 17 March 2021)

Second-order photonic topological insulators that host highly localized corner states resilient to defects, are opening alternative routes towards developing fascinating photonic devices. However, the existing works on second-order photonic topological insulators have mainly focused on either transverse-magnetic or transverse-electric modes. In this paper, we propose a dual-polarization topological photonic crystal structure for both transverse magnetic and transverse electric modes through topology optimization. Simple tight-binding lattice models are constructed to reveal the topological features of the optimized photonic crystal structure in a transparent way. The optimized dual-polarization second-order photonic topological insulator hosts four groups of corner states with different profiles and eigenfrequencies for both the transverse-magnetic and transverse-electric modes. Moreover, the robustness of these corner states against defects is explicitly demonstrated. Our results offer opportunities for developing polarization-independent topological photonic devices.

DOI: 10.1103/PhysRevApplied.15.034053

I. INTRODUCTION

One of the most noteworthy recent developments of condensed-matter physics is the discovery of topological states of matter [1–5], in particular, topological insulators (TIs) [6,7]. A unique feature of these systems is the existence of topological protected edge states, where according to the bulk-edge correspondence principle, a d -dimensional TI supports ($d-1$) dimensional gapless edge states. Inspired by the interesting physics and promising technological applications, the concept of TIs has been extended to classical wave systems, e.g., photonic systems [8–17]. Photonic topological insulators enable the robust manipulation of light, thus providing the possibility of alternative topological photonic applications, such as non-reciprocal devices [11], pseudospin-polarized waveguides [12–14], and topological lasers [18–20].

Beyond the traditional bulk-boundary correspondence, high-order TIs can host lower-dimensional boundary states [21–23]. For example, a d -dimensional second-order TI

supports ($d-1$) dimensional gapped boundary states but ($d-2$) dimensional gapless edge states, which are corner states in two-dimensional (2D) systems. The second-order photonic TIs (SPTIs) have been theoretically predicted and experimentally demonstrated [24–30]. Based on these highly localized corner states, a high- Q -factor nanocavity [31] and low-threshold topological nanolaser [32] have been experimentally realized.

For 2D photonic crystals (PtCs), electromagnetic waves possess two possible polarizations, i.e., transverse-magnetic (TM) modes or transverse-electric (TE) modes. So far, the existing works of SPTIs have focused on either TM or TE modes. Thus it would be interesting to see whether SPTIs for both the TM and TE modes, i.e., dual polarization, could be built considering the fact that polarization-dependent manipulation of light is a relevant and active area of research in photonics [33], which has many practical applications. For example, low-threshold topological nanolasers based on second-order corner states have been demonstrated recently [32]. A dual-polarization SPTI would allow the realization of the so-called dual-polarization laser [34–36] with additional built-in topological protection. Furthermore, due to the significant difference between the field distributions of TE and TM polarization modes, which respond differently

*z.lan@ucl.ac.uk

†bjiag@swin.edu.au

‡xhuang@swin.edu.au

§These authors contributed equally to this work.

to the environment, dual-polarization interferometry has been widely used for a broad range of applications [37–39], such as, bionanotechnology, surface science, liquid studies, crystallography, and drug discovery. Dual polarization is also useful to enhance nonlinear optical effects [40–45]. For example, in nonlinear optics, materials with large off-diagonal nonlinear susceptibility terms can be used to enhance the harmonic generation when two modes with orthogonal polarizations are mixed [41]. Last but not least, polarization division multiplexing [46] is widely used in high-speed communication systems due to its ability to enlarge the capacity and data rates of these systems and as such devices, like, dual-polarization modulator [47–49], transmitter [50,51], and receiver [52–54] are actively explored for realizing dual-polarization photonic integrated circuits.

Considering the usefulness of dual-polarization optics and its diverse applications, in this work, we propose an alternative dual-polarization SPTI supporting corner states based on an optimized PtC structure with a wide complete band gap (CBG). Interestingly, we find that two different choices of the unit cell (UC) for the optimized PtC exhibit distinct topological properties for both the TM and TE modes, where the numerical results are confirmed by simple tight-binding analysis. SPTIs can be built by forming edges and corners between the topologically trivial and nontrivial unit cells. We find that the created SPTI hosts four groups of corner states with different eigenfrequencies and field profiles for both the TM and TE modes. Moreover, the robustness of these corner states against defects is also verified. The proposed dual-polarization SPTI could provide a promising platform for the development of polarization-independent topological photonic applications.

II. DESIGN OF THE DUAL-POLARIZATION SPTI

Since the corner states generally locate within the frequency band gap, designing a PtC with a CBG is the prerequisite for constructing a dual-polarization SPTI. However, dielectric material of PtC with a band gap in the TM modes usually consists of isolated dielectric “rods,” while it forms “walls” for the TE modes. This opposite structural characteristics makes it challenging to create a PtC with a CBG for the TM and TE modes simultaneously. To tackle this design problem, we consider a PtC structure composed of GaAs with $\epsilon_r = 11.4$ and air with $\epsilon_r = 1$ and employ the topology optimization method. In this method, we firstly design a PtC with a complete band gap for both TM and TE modes and set the gap-midgap ratio as the objective function. We then discretize the unit cell uniformly into 96×96 square elements and treat each element as the design variable. Upon calculating the sensitivity of the objective function with respect to each design variable, the optimization algorithm increases design variables for

elements with high sensitivities and decreases design variables for elements with low sensitivities iteratively until the objective function is maximized (for more details of the numerical optimization algorithm, see Ref. [55]). Figures 1(a) and 1(b) show one of the optimized PtCs with a maximal CBG and its band structure for both the TM and TE modes, respectively. The gap-midgap ratio of the CBG is 20.79% with the band gap ranging from the normalized frequency of 0.726 to 0.894. This CBG exists from an overlap of the TM band gap between bands 9 and 10 with the TE band gap between bands 5 and 6.

For the topological properties of our optimized PtC structure, while previous studies based on the 2D Su-Schrieffer-Heeger (SSH) model suggest that choosing the unit cell in different ways could result in different topological behaviors [24–27,31,56–58], it is a nontrivial question whether our PtC will exhibit any topological properties because our system is not based on the SSH design. To study the topological properties of our optimized PtC, we select two different UCs (UC1 and UC2) as sketched in Fig. 1(a), where UC1 is the primitive unit cell of the optimized PtC while UC2 is a translation of UC1 by $(a/2, a/2)$ with a the lattice constant. The topological properties of UC1 and UC2 could be characterized by the 2D polarization $\mathbf{P} = (P_x, P_y)$ defined by [57]

$$P_i = \frac{1}{2} \left(\sum_n q_i^n \text{modulo}2 \right), \quad (-1)^{q_i^n} = \frac{\eta_n(X_i)}{\eta_n(\Gamma)}, \quad (1)$$

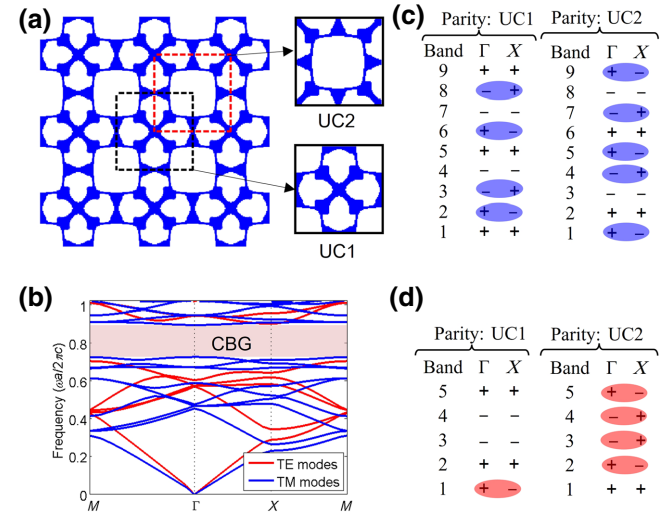


FIG. 1. (a) Structure of the optimized PtC considered in this work and two different choices of the unit cell, i.e., UC1 and UC2. (b) Band structure of the PtC with a CBG. Parities of bands below the CBG at high symmetric points Γ and X of the first Brillouin zone for TM (c) and TE (d) modes, respectively, where an odd number of pairs of parities with opposite signs at Γ and X of the same band below the gap indicates the gap is topological nontrivial whereas an even number implies a trivial gap.

where $i = x, y$ stands for the direction and η_n represents the parity at the high-symmetry points $\Gamma = (0, 0)$ and $X = \pi/a(1, 0)$ of the first Brillouin zone for the n th band. Note due to the C_{4v} point group symmetry of our PtC structure, \mathbf{P} could be determined by the parities at the high-symmetric points [57,59,60] and also $P_x = P_y$.

The parities at the high-symmetric points of UC1 and UC2 for both TM and TE modes are shown in Figs. 1(c) and 1(d), respectively. The corresponding eigenmode profiles used for identifying the parities are given in the appendix, from which one can determine the parity by the behavior of the eigenmode profile under the inversion operation with respect to the center of the unit cell. In this way, one can find that the p modes have an odd parity ($-$), whereas the s and d modes have an even parity ($+$). According to the results of Figs. 1(c) and 1(d) and Eq. (1), which indicate that an odd number of pairs of parities with opposite signs at Γ and X of the same band below the gap makes the gap topological nontrivial whereas an even number implies the gap is trivial, the 2D polarizations of UC1 and UC2 can be determined to be $\mathbf{P} = (0, 0)$ and $\mathbf{P} = (\frac{1}{2}, \frac{1}{2})$, respectively, for the TM modes, and $\mathbf{P} = (\frac{1}{2}, \frac{1}{2})$ and $\mathbf{P} = (0, 0)$ for the TE modes. This means that UC1 is trivial and UC2 is nontrivial for the TM modes, while UC1 is nontrivial and UC2 is trivial for the TE modes, which is fully compatible with the complementary nature of TM and TE modes. Based on the 2D polarizations, the topological corner charge can be calculated as [59,60],

$$Q^c = 4P_xP_y. \quad (2)$$

As a result, the corner charges of (UC1, UC2) are $(0, 1)$ for the TM modes, and $(1, 0)$ for the TE modes.

While we show above that the optimized PtC can exhibit topological properties through numerical calculations of the band structure and eigenmode profiles, it would be more insightful if a simple tight-binding lattice model could be built to understand these interesting topological features as this would allow us to demonstrate that the topological features of the optimized PtC structure exist at a more fundamental level, i.e., applicable to any systems that can effectively implement the lattice model.

To this end, we note that while the dielectric regions can be viewed as lattice sites for the TM modes, air regions serve this purpose for the TE modes. As such, the lattice models for the TM and TE modes can readily be constructed, which are presented in Figs. 2(a) and 2(d). Particles hopping in these lattices can be described by the following Hamiltonian:

$$H = - \sum_{\langle ij \rangle} t_{ij} c_i^\dagger c_j, \quad (3)$$

where the hopping patterns (t_{ij}) for the TM and TE modes are also given in Figs. 2(a) and 2(d), respectively, and

c_i^\dagger (c_i) is the creation (annihilation) operator of the particle at site i . Note, to match more closely with the PtC structure in Fig. 1(a), three hopping strengths of t_0, t_1, t_2 are introduced. The values of t_0, t_1, t_2 in the tight-binding models could be chosen in the following way. First, from the topology-optimized PtC structure shown in Fig. 1(a) and its tight-binding pictures in Figs. 2(a) and 2(d), one can roughly identify the relation among t_0, t_1, t_2 . For example, for the TM modes, as the dielectric connection for t_0 is a thin stripe, it is smaller than t_1 and t_2 . Moreover, one can also see that the dielectric connection for t_1 is thicker than t_2 , thus, $t_1 > t_2$. Based on these intuitive relations, one can scan the values of t_0, t_1, t_2 in the tight-binding models directly and choose these values that give the band structures in Figs. 2(b) and 2(e) as closer as these in Fig. 1(b). The resulting tight-binding band structures for the TM and TE modes are given in Figs. 2(b) and 2(e), respectively, which reproduce the PtC band structures in Fig. 1(b) qualitatively. The lattice structure for the TM modes contains nine lattice sites in each unit cell while it contains five lattice sites for the TE modes, thus there are nine bands for the TM modes and five bands for the TE modes, which perfectly agrees with the number of bands below the CBG for both the TM and TE modes. The lattices in Figs. 2(a)

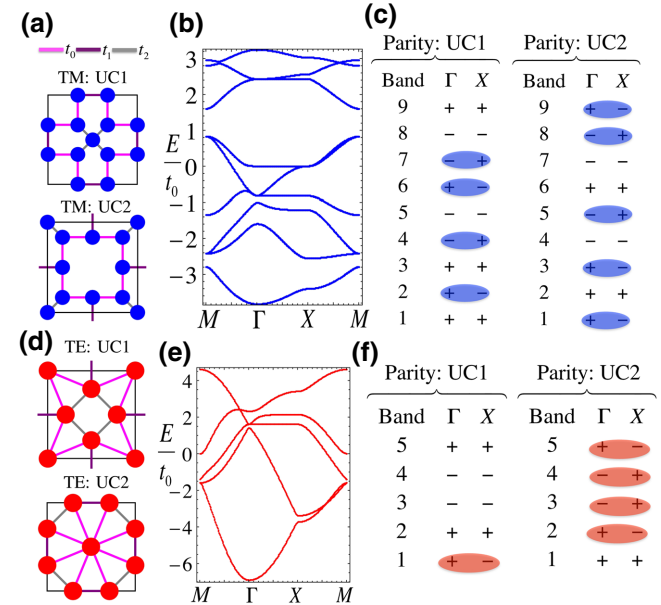


FIG. 2. (a) Tight-binding unit cells (UC1, UC2) for the TM modes with three different kinds of hopping t_0, t_1, t_2 . (b) The tight-binding band structure for the TM modes with $t_0 = 1, t_1 = 1.6, t_2 = 1.4$. (c) Parity distribution of the nine bands at the high-symmetry points of Γ and X for the two different unit cells in (a). (d) Tight-binding unit cells (UC1, UC2) for the TE modes. (e) The tight-binding band structure for the TE modes with $t_0 = 1, t_1 = 1.6, t_2 = 1.5$. (f) Parity distribution of the five bands at the high-symmetry points of Γ and X for the two different unit cells in (d).

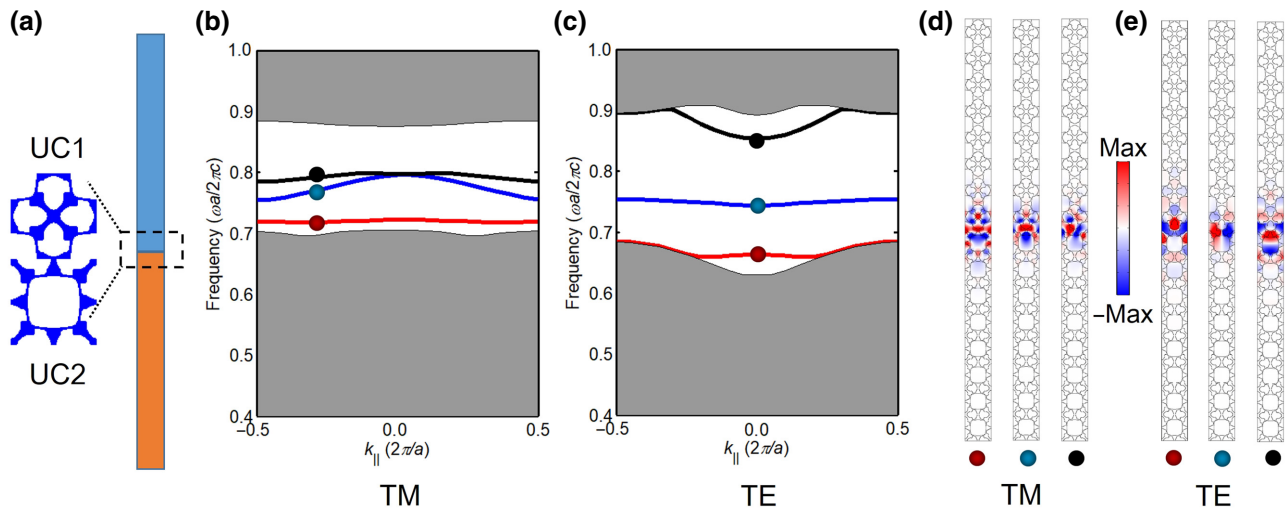


FIG. 3. (a) Schematic of the supercell of a ribbon structure, which is periodic along the horizontal direction and consists of eight UC1s and eight UC2s with a domain wall between them. (b),(c) Projected band structures of the ribbon for the TM and TE modes, respectively. The solid lines within the gap indicate the emerging topological edge states while gray regions mark the bulk states. (d),(e) Eigenfield profiles at the solid points in (b),(c) for TM and TE modes, respectively, which demonstrate the highly localized nature of these modes.

and 2(d) possess the inversion symmetry, which allows the states at inversion symmetric points (such as Γ and X) to associate with a definite parity. Figures 2(c) and 2(f) show the parity distributions at the high-symmetry points Γ and X . While the tight-binding band structure and parity distribution for TE modes match these of the PtC structure in Fig. 1, we can not find parameters of t_0, t_1, t_2 that reproduce the parity distribution of the PtC structure for the TM modes as there are more bands for the TM modes than the TE modes, thus requiring a higher degree of fine tuning. Another possibility is that, the long-range hopping physics of the electromagnetic waves in the PtC structure is not captured by our simple tight-binding description with only three short-range hopping terms. Nevertheless, the topological invariants (odd or even number of pairs of parities with opposite signs at Γ and X for the same band) for the TM modes are the same as these of the PtC structure.

It is interesting to note that our lattice models have an odd number of bands (i.e., nine bands for the TM modes and five for the TE) and the whole band structure (i.e., considered gap above all bands) possesses topological behavior for one choice of the unit cell, which is very different from the widely used 2D SSH square tight-binding lattice model (see, e.g., Ref. [57]), which has an even number of bands and the whole band structure is topological trivial for both choices of the unit cell, i.e., one would need to consider partially filled bands of the 2D square SSH model for topological applications.

III. TOPOLOGICAL EDGE AND CORNER STATES

According to the bulk-edge correspondence principle, topological edge states will emerge at the boundary

between topological trivial and nontrivial PtCs. To verify the existence of topological edge states, we consider a ribbon structure consisting of eight UC1s and eight UC2s with a domain wall between them, as illustrated in Fig. 3(a). Figures 3(b) and 3(c) show the projected band structures for the TM and TE modes, respectively, from which one can see that three waveguide modes appear within the CBG. Figures 3(d) and 3(e) further present the eigenfields of the edge states calculated at the solid points in Figs. 3(b) and 3(c) for the TM and TE modes, respectively. As can be seen, these modes are highly localized at the edge between UC1 and UC2, which could be used as defect-immune light transport. Of note, these edge states are gapped, which is also the prerequisite for the generation of topological corner states [59,60].

The different corner charges between UC1 and UC2 guarantee the existence of topological corner states. To further demonstrate the coexistence of topological edge and corner states, we build a box-shaped region consisting of 10×10 UC2s surrounded by three-layer UC1s, as sketched in Fig. 4(a). Figures 4(b) and 4(c) plot the calculated eigenfrequencies of the finite-size structure for TM and TE modes, respectively, from which one can see the coexistence of topological edge and corner states within the CBG for both the TM and TE modes. Figures 4(d) and 4(e) show the typical eigenfield distributions of the edge states for the TM and TE modes, respectively. It can be seen that electromagnetic waves are highly localized at the domain wall between UC1 and UC2. It is interesting to note that the proposed SPTI hosts four groups of corner states at different frequencies, which are labeled as TMC1, TMC2, TMC3, TMC4 for the TM modes and

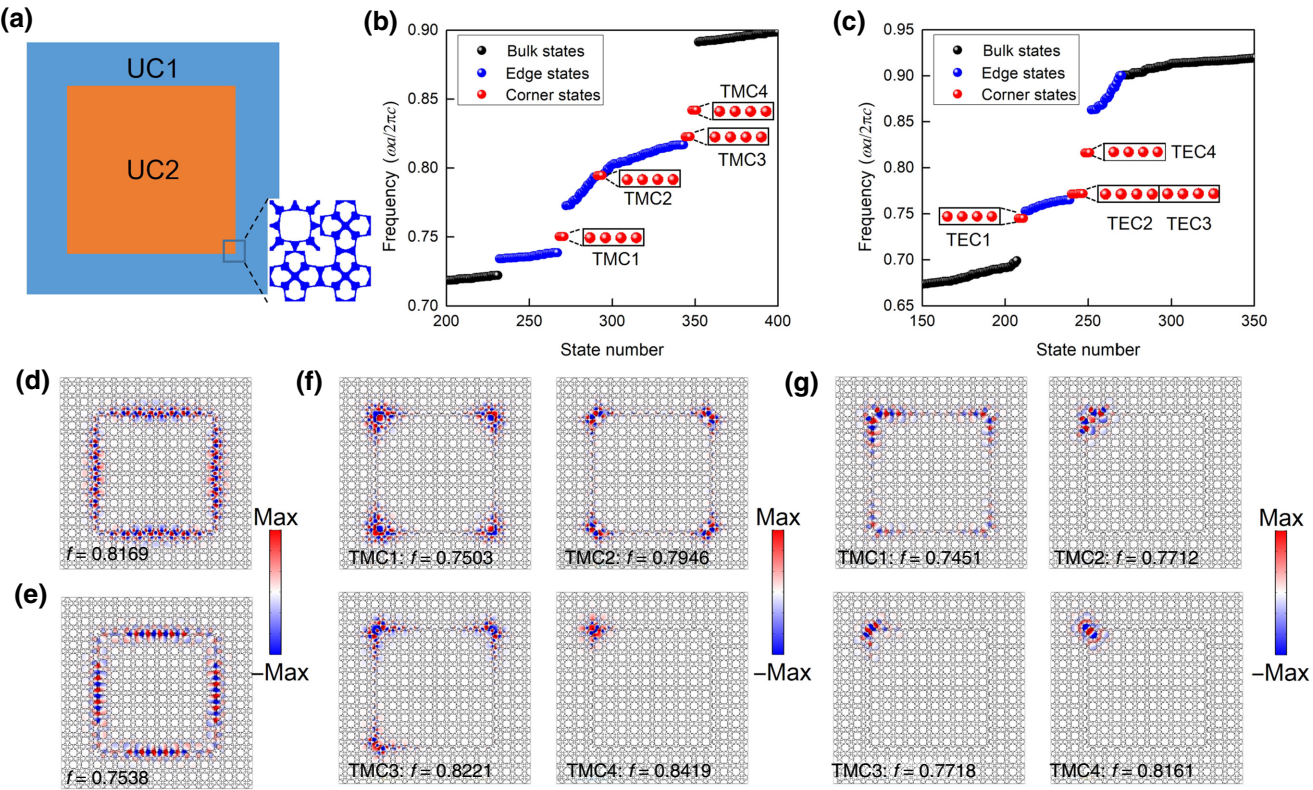


FIG. 4. (a) Schematic of a box-shaped finite-size structure consisting of 10×10 UC2s surrounded by three-layer UC1s for the study of coexistence of topological edge and corner states. (b),(c) Calculated eigenfrequencies of the box-shaped structure for the TM and TE modes, respectively, where four groups of corner states emerge within the CBG for both the TM and TE modes. (d),(e) Typical eigenfield profiles of the edge states for the TM and TE modes, respectively (note $f = \omega a/2\pi c$). (f),(g) Eigenfield distributions of one representative corner state in each of the four groups for the TM and TE modes, respectively.

TEC1, TEC2, TEC3, TEC4 for the TE modes in Figs. 4(b) and 4(c), respectively. As a result, our current design of the SPTI is distinct from any existing SPTIs, which only host one or two groups of corner states. Figures 4(f) and

4(g) show the eigenfield distributions of the corner states for TM and TE modes, respectively. Each group of corner states contains four degenerate corner states, therefore only one eigenfield distribution of a representative corner state

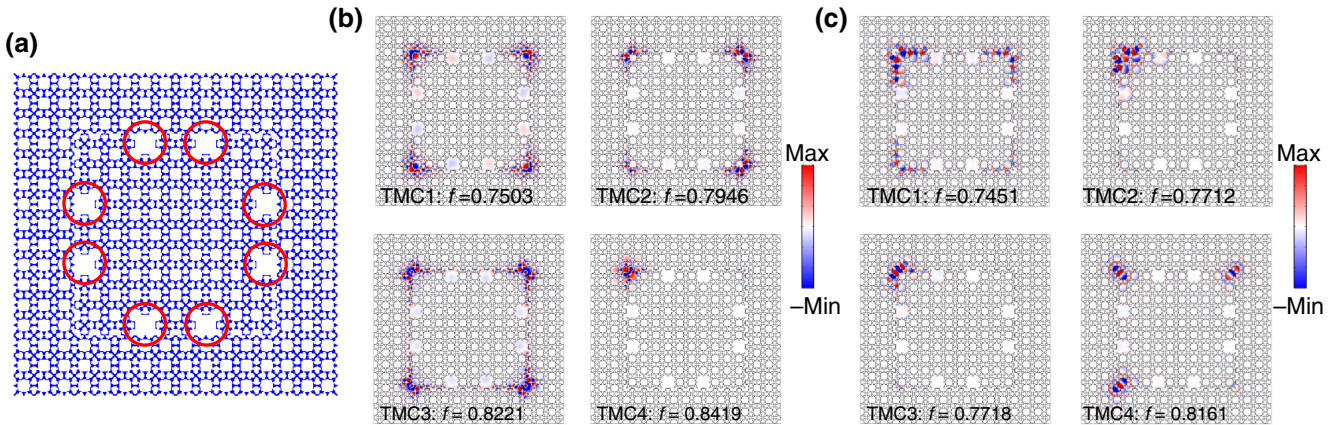


FIG. 5. (a) Schematic of a perturbed structure after removing certain UCs denoted by the red circles for the demonstration of robustness of the corner states against defect. (b),(c) Calculated eigenfields and eigenfrequencies of one representative corner state from each of the four groups for the TM and TE modes, respectively.

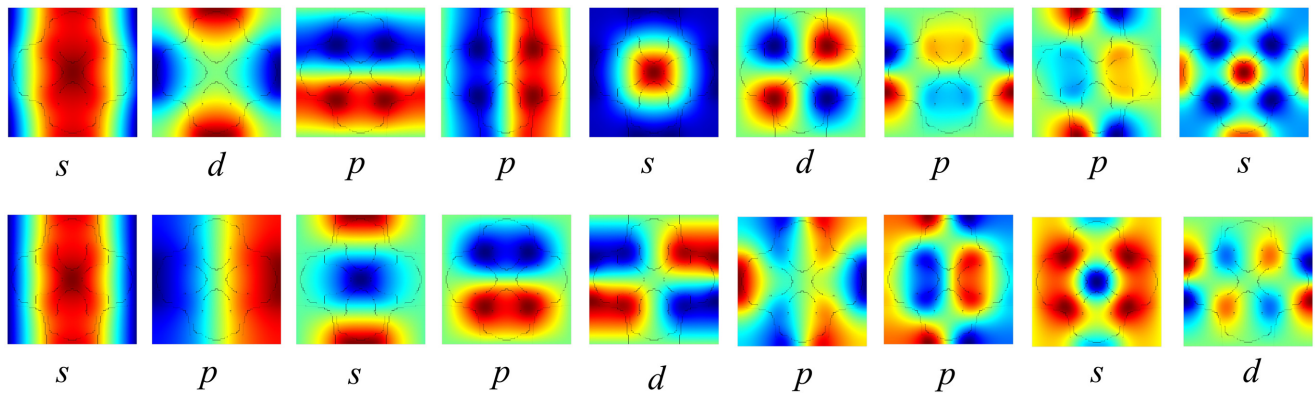


FIG. 6. Eigenmode profiles at Γ point (upper panel) and X point (bottom panel) for the nine bands (from left to right) of UC1 in TM modes.

in each group is plotted. It reveals that these corner states are highly localized around the corners and exhibit different profiles, which may provide flexibilities in practical applications.

The corner states have a topological origin related to the different corner charges of UC1 and UC2, thus they enjoy the topological protection. To demonstrate the robustness of the corner states against defects, we remove some unit cells around the corners as denoted by the red circles in Fig. 5(a). The eigenfields and eigenfrequencies of the corner states in this perturbed structure are calculated and presented in Figs. 5(b) and 5(c) for the TM and TE modes, respectively. As can be seen, although defects are introduced around the corners, all the corner states remain unchanged and their eigenfrequencies also keep invariant, demonstrating the robustness of the corner states against defects.

IV. CONCLUSION

In conclusion, we demonstrate the design of a dual-polarization SPTI, which supports localized corner states for both the TM and TE modes in a wide common gap. Our design is based on the topology optimization method and the topological properties of the optimized PtC structure are characterized through the band structures and parity analysis of the eigenmode profiles. The designed SPTI hosts four groups of corner states with different eigenfrequencies and field profiles for both the TM and TE modes, which provide more degrees of freedom for developing new photonic devices compared to the existing SPTIs. We also demonstrate the robustness of these corner states against defects, which could advance the design of polarization-independent topological devices with diverse functionalities.

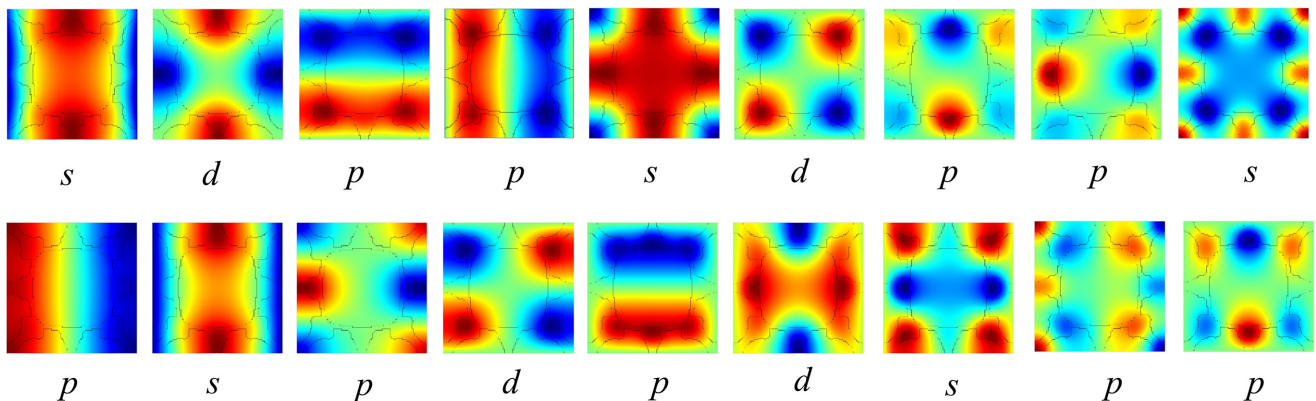


FIG. 7. Eigenmode profiles at Γ point (top panel) and X point (bottom panel) for the nine bands (from left to right) of UC2 in TM modes.

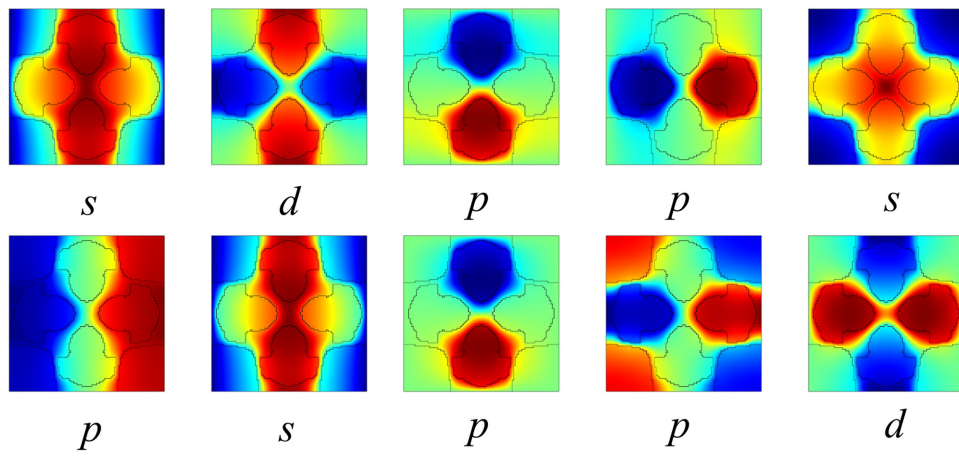


FIG. 8. Eigenmode profiles at Γ point (upper panel) and X point (bottom panel) for the five bands (from left to right) of UC1 in TE modes.

Moreover, we construct simple tight-binding lattice models, which allow us to capture the key topological features of the optimized PtC structure in a transparent way and these tight-binding lattice models indicate that the dual-polarization topological physics we reveal in the PtC system carries over to diverse system platforms, such as plasmonics, acoustics, as long as these systems can implement the tight-binding models. Furthermore, these tight-binding lattice models have an odd number of lattice sites in each unit cell and the whole band structure shows topological properties for one choice of the unit cell. These interesting features are beyond the 2D square SSH paradigm, which has an even number of lattice sites in its unit cell and the whole band structure shows no topological properties for both choices of the unit cell, i.e., one would need to consider partially filled bands of the 2D square SSH model for topological applications, which may limit

the size of the topological band gap. Thus we expect our findings will bring alternative insights and open interesting directions in this field. Finally, we note that it is certainly interesting to see whether dual-polarization SPTI can be constructed in PtCs having hexagonal symmetry [61–63].

ACKNOWLEDGMENTS

The authors thank Professor Yuri Kivshar at the Non-linear Physics Center, Australian National University for valuable feedback. The authors also wish to acknowledge the support from the Hong Kong Scholars Program (Grant No. XJ2020004), the Australian Research Council through the Discovery Project schemes (DP210103523; DP190103186) and the Industrial Transformation Training Centres scheme (IC180100005).

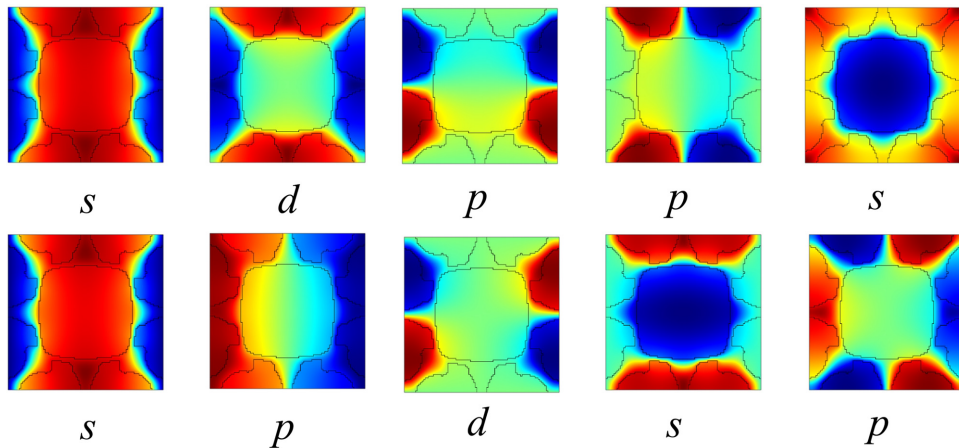


FIG. 9. Eigenmode profiles at Γ point (upper panel) and X point (bottom panel) for the five bands (from left to right) of UC2 in TE modes.

APPENDIX: EIGENMODE PROFILES OF THE OPTIMIZED PtC AT HIGH-SYMMETRY POINTS Γ AND X

In this appendix, we give the eigenmode profiles of the optimized PtC at high-symmetry points of Γ and X , whose parities under the inversion operation are listed in Figs. 1(c) and 1(d) and used for determination of the topological properties of UC1 and UC2 through Eq. (1). In particular, Figs. 6 and 7 show the TM eigenmode profiles of the nine bands at the high-symmetry points of Γ and X for UC1 and UC2, respectively. On the other hand, Figs. 8 and 9 show the TE eigenmode profiles of the five bands at the high-symmetry points of Γ and X for UC1 and UC2, respectively. Note, for the eigenmode profiles presented in Figs. 6–9, while the p modes have an odd parity (−), the s and d modes have an even parity (+).

-
- [1] D. J. Thouless, M. Kohmoto, M. P. Nightingale, and M. den Nijs, Quantized Hall Conductance in a Two-Dimensional Periodic Potential, *Phys. Rev. Lett.* **49**, 405 (1982).
- [2] K. v. Klitzing, G. Dorda, and M. Pepper, New Method for High-Accuracy Determination of the Fine-Structure Constant Based on Quantized Hall Resistance, *Phys. Rev. Lett.* **45**, 494 (1980).
- [3] F. D. M. Haldane, Model for a Quantum Hall Effect Without Landau Levels: Condensed-Matter Realization of the “Parity Anomaly”, *Phys. Rev. Lett.* **61**, 2015 (1988).
- [4] C. L. Kane and E. J. Mele, Quantum Spin Hall Effect in Graphene, *Phys. Rev. Lett.* **95**, 226801 (2005).
- [5] C.-Z. Chang, J. Zhang, X. Feng, J. Shen, Z. Zhang, M. Guo, K. Li, Y. Ou, P. Wei, L.-L. Wang, Z-Q. Ji, Y. Feng, S. Ji, X. Chen, J. Jia, X. Dai, Z. Fang, S.-C. Zhang, K. He, Y. Wang, L. Lu, X.-C. Ma, and Q.-K. Xue, Experimental observation of the quantum anomalous hall effect in a magnetic topological insulator, *Science* **340**, 167 (2013).
- [6] M. Z. Hasan and C. L. Kane, Colloquium: Topological insulators, *Rev. Mod. Phys.* **82**, 3045 (2010).
- [7] X.-L. Qi and S.-C. Zhang, Topological insulators and superconductors, *Rev. Mod. Phys.* **83**, 1057 (2011).
- [8] A. B. Khanikaev and G. Shvets, Two-dimensional topological photonics, *Nat. Photonics* **11**, 763 (2017).
- [9] T. Ozawa, H. M. Price, A. Amo, N. Goldman, M. Hafezi, L. Lu, M. C. Rechtsman, D. Schuster, J. Simon, O. Zilberberg, and I. Carusotto, Topological photonics, *Rev. Mod. Phys.* **91**, 015006 (2019).
- [10] F. D. M. Haldane and S. Raghu, Possible Realization of Directional Optical Waveguides in Photonic Crystals with Broken Time-Reversal Symmetry, *Phys. Rev. Lett.* **100**, 013904 (2008).
- [11] Z. Wang, Y. D. Chong, J. D. Joannopoulos, and M. Soljacic, Observation of unidirectional backscattering-immune topological electromagnetic states, *Nature* **461**, 772 (2009).
- [12] L.-H. Wu and X. Hu, Scheme for Achieving a Topological Photonic Crystal by Using Dielectric Material, *Phys. Rev. Lett.* **114**, 223901 (2015).
- [13] Y. Yang, Y. F. Xu, T. Xu, H.-X. Wang, J.-H. Jiang, X. Hu, and Z. H. Hang, Visualization of a Unidirectional Electromagnetic Waveguide Using Topological Photonic Crystals Made of Dielectric Materials, *Phys. Rev. Lett.* **120**, 217401 (2018).
- [14] M. L. N. Chen, L. J. Jiang, Z. Lan, and W. E. I. Sha, Pseudospin-polarized topological line defects in dielectric photonic crystals, *IEEE Trans. Antennas Propag.* **68**, 609 (2020).
- [15] X. Zhu, H.-X. Wang, C. Xu, Y. Lai, J.-H. Jiang, and S. John, Topological transitions in continuously deformed photonic crystals, *Phys. Rev. B* **97**, 085148 (2018).
- [16] L. Xu, H.-X. Wang, Y.-D. Xu, H.-Y. Chen, and J.-H. Jiang, Accidental degeneracy in photonic bands and topological phase transitions in two-dimensional core-shell dielectric photonic crystals, *Opt. Express* **24**, 18059 (2016).
- [17] Y. Chen, F. Meng, B. Jia, G. Li, and X. Huang, Inverse design of photonic topological insulators with extra-wide bandgaps, *Phys. Status Solidi RRL* **13**, 1900175 (2019).
- [18] B. Bahari, A. Ndao, F. Vallini, A. El Amili, Y. Fainman, and B. Kante, Nonreciprocal lasing in topological cavities of arbitrary geometries, *Science* **358**, 636 (2017).
- [19] G. Harari, M. A. Bandres, Y. Lumer, M. C. Rechtsman, Y. D. Chong, M. Khajavikhan, D. N. Christodoulides, and M. Segev, *Topological insulator laser: Theory*, *Science* **359**, eaar4003 (2018).
- [20] M. A. Bandres, S. Wittek, G. Harari, M. Parto, J. Ren, M. Segev, D. N. Christodoulides, and M. Khajavikhan, *Topological insulator laser: Experiments*, *Science* **359**, eaar4005 (2018).
- [21] F. Schindler, A. M. Cook, M. G. Vergniory, Z. Wang, S. S. P. Parkin, B. Andrei Bernevig, and T. Neupert, *Higher-order topological insulators*, *Sci. Adv.* **4**, eaat0346 (2018).
- [22] W. A. Benalcazar, A. Bernevig, and T. L. Hughes, Quantized electric multipole insulators, *Science* **357**, 61 (2017).
- [23] W. A. Benalcazar, B. A. Bernevig, and T. L. Hughes, Electric multipole moments, topological multipole moment pumping, and chiral hinge states in crystalline insulators, *Phys. Rev. B* **96**, 245115 (2017).
- [24] B.-Y. Xie, H.-F. Wang, H.-X. Wang, X.-Y. Zhu, J.-H. Jiang, M.-H. Lu, and Y.-F. Chen, Second-order photonic topological insulator with corner states, *Phys. Rev. B* **98**, 205147 (2018).
- [25] B.-Y. Xie, G.-X. Su, H.-F. Wang, H. Su, X.-P. Shen, P. Zhan, M.-H. Lu, Z.-L. Wang, and Y.-F. Chen, Visualization of Higher-Order Topological Insulating Phases in Two-Dimensional Dielectric Photonic Crystals, *Phys. Rev. Lett.* **122**, 233903 (2019).
- [26] X.-D. Chen, W.-M. Deng, F.-L. Shi, F.-L. Zhao, M. Chen, and J.-W. Dong, Direct Observation of Corner States in Second-Order Topological Photonic Crystal Slabs, *Phys. Rev. Lett.* **122**, 233902 (2019).
- [27] A. El Hassan, F. K. Kunst, A. Moritz, G. Andler, E. J. Bergholtz, and M. Bourennane, Corner states of light in photonic waveguides, *Nat. Photonics* **13**, 697 (2019).
- [28] Y. Chen, F. Meng, Y. Kivshar, B. Jia, and X. Huang, Inverse design of higher-order photonic topological insulators, *Phys. Rev. Res.* **2**, 023115 (2020).
- [29] H.-R. Kim, M.-S. Hwang, D. Smirnova, K.-Y. Jeong, Y. Kivshar, and H.-G. Park, Multipolar lasing modes from topological corner states, *Nat. Commun.* **11**, 5758 (2020).
- [30] S. Mittal, V. V. Orre, G. Zhu, M. A. Gorlach, A. Poddubny, and M. Hafezi, Photonic quadrupole topological phases, *Nat. Photonics* **13**, 692 (2019).

- [31] Y. Ota, F. Liu, R. Katsumi, K. Watanabe, K. Wakabayashi, Y. Arakawa, and S. Iwamoto, Photonic crystal nanocavity based on a topological corner state, *Optica* **6**, 786 (2019).
- [32] W. Zhang, X. Xie, H. Hao, J. Dang, S. Xiao, S. Shi, H. Ni, Z. Niu, C. Wang, K. Jin, X. Zhang, and X. Xu, Low-threshold topological nanolasers based on the second-order corner state, *Light Sci. Appl.* **9**, 109 (2020).
- [33] D. Dai, L. Liu, S. Gao, D.-X. Xu, and S. He, Polarization management for silicon photonic integrated circuits, *Laser Photonics Rev.* **7**, 303 (2013).
- [34] J. Thevenin, M. Vallet, and M. Brunel, Dual-polarization mode-locked Nd:YAG laser, *Opt. Lett.* **37**, 2859 (2012).
- [35] T. Mueller, A. Maese-Novo, Z. Zhang, A. Polatynski, D. Felipe, M. Kleinert, W. Brinker, C. Zawadzki, and N. Keil, Switchable dual-polarization external cavity tunable laser, *Opt. Lett.* **40**, 447 (2015).
- [36] M. Guionie, M. Romanelli, A. Thorette, A. Carre, E. Pinsard, L. Lablonde, B. Cadier, M. Alouini, M. Vallet, and M. Brunel, Delay-induced instability in phase-locked dual-polarization distributed-feedback fiber lasers, *Phys. Rev. A* **101**, 043843 (2020).
- [37] J. Escorihuela, M. A. G.-Martinez, J. L. L.-Paz, R. Puchades, A. Maqueira, and D. G.-Romero, Dual-polarization interferometry: A novel technique to light up the nanomolecular world, *Chem. Rev.* **115**, 265 (2015).
- [38] A. Psarouli, A. Salapatas, A. Botsialas, P. S. Petrou, I. Raptis, E. Makarona, G. Jobst, K. Tukkiniemi, M. Sopanen, R. Stoffer, S. E. Kakabakos, and K. Misiakos, Monolithically integrated broad-band Mach-Zehnder interferometers for highly sensitive label-free detection of biomolecules through dual polarization optics, *Sci. Rep.* **5**, 17600 (2015).
- [39] R. A. Abram and S. Brand, Some theory of a dual-polarization interferometer for sensor applications, *J. Phys. D: Appl. Phys.* **48**, 125101 (2015).
- [40] A. C. Lesina, L. Ramunno, and P. Berini, Dual-polarization plasmonic metasurface for nonlinear optics, *Opt. Lett.* **40**, 2874 (2015).
- [41] Y. Zhang, M. W. McCutcheon, I. B. Burgess, and M. Loncar, Ultra-high-Q TE/TM dual-polarized photonic crystal nanocavities, *Opt. Lett.* **34**, 2694 (2009).
- [42] C.-S. Deng, Y.-S. Gao, X.-Z. Wu, M.-J. Li, and J.-X. Zhong, Ultrahigh-Q TE/TM dual-polarized photonic crystal holey fishbone-like nanobeam cavities, *EPL* **108**, 54006 (2014).
- [43] M. Minkov, D. Gerace, and S. Fan, Doubly resonant χ (2) nonlinear photonic crystal cavity based on a bound state in the continuum, *Optica* **6**, 1039 (2019).
- [44] D. Smirnova, D. Leykam, Y. Chong, and Y. Kivshar, Nonlinear topological photonics, *Appl. Phys. Rev.* **7**, 021306 (2020).
- [45] W. G. Sergey Kruk, D. Y. Choi, T. Zentgraf, S. Zhang, and Y. Kivshar, Nanoscale topological corner states in nonlinear optics, *arXiv:2011.10164* (2020).
- [46] D. Dai and J. E. Bowers, Silicon-based on-chip multiplexing technologies and devices for Peta-bit optical interconnects, *Nanophotonics* **3**, 283 (2014).
- [47] X. Li, A. Wen, W. Chen, Y. Gao, S. Xiang, H. Zhang, and X. Ma, Photonic Doppler frequency shift measurement based on a dual-polarization modulator, *Appl. Opt.* **56**, 2084 (2017).
- [48] X. Qiu, X. Ruan, Y. Li, and F. Zhang, Indium tin oxide based dual-polarization electro-optic intensity modulator on a single silicon waveguide, *J. Light. Technol.* **36**, 2563 (2018).
- [49] R. Zheng, E. H. W. Chan, X. Wang, X. Feng, and B. Guan, Broadband high dynamic range fiber optic link based on a dual-polarization modulator, *Opt. Express* **27**, 4734 (2019).
- [50] Q. Zhang, Y. Yang, C. Guo, X. Zhou, Y. Yao, A. P. T. Lau, and C. Lu, Modulation-format-transparent IQ imbalance estimation of dual-polarization optical transmitter based on maximum likelihood independent component analysis, *Opt. Express* **27**, 18055 (2019).
- [51] A. H. Ahmed, A. El Moznine, D. Lim, Y. Ma, A. Rylyakov, and S. Shekhar, A dual-polarization silicon-photonic coherent transmitter supporting 552 Gb/s/wavelength, *IEEE J. Solid-State Circuits* **55**, 2597 (2020).
- [52] C. Alonso-Ramos, P. J. Reyes-Iglesias, A. Ortega-Monux, D. Perez-Galacho, R. Halir, and I. Molina-Fernandez, Polarization-beam-splitter-less integrated dual-polarization coherent receiver, *Opt. Lett.* **39**, 4400 (2014).
- [53] J. Lu, X. Li, S. Fu, M. Luo, M. Xiang, H. Zhou, M. Tang, and D. Liu, Joint carrier phase and frequency-offset estimation with parallel implementation for dual-polarization coherent receiver, *Opt. Express* **25**, 5217 (2017).
- [54] C. Clivati, P. Savio, S. Abrate, V. Curri, R. Gaudino, M. Pizzocaro, and D. Calonico, Robust optical frequency dissemination with a dual-polarization coherent receiver, *Opt. Express* **28**, 8494 (2020).
- [55] F. Meng, S. Li, Y. Li, B. Jia, and X. Huang, Microstructural design for 2D photonic crystals with large polarization-independent band gaps, *Mater. Lett.* **207**, 176 (2017).
- [56] Z.-G. Chen, C. Xu, R. Al Jahdali, J. Mei, and Y. Wu, Corner states in a second-order acoustic topological insulator as bound states in the continuum, *Phys. Rev. B* **100**, 075120 (2019).
- [57] F. Liu and K. Wakabayashi, Novel Topological Phase with a Zero Berry Curvature, *Phys. Rev. Lett.* **118**, 076803 (2017).
- [58] F. Meng, Y. Chen, W. Li, B. Jia, and X. Huang, Realization of multidimensional sound propagation in 3D acoustic higher-order topological insulator, *Appl. Phys. Lett.* **117**, 151903 (2020).
- [59] Z. Zhang, M. R. Lopez, Y. Cheng, X. Liu, and J. Christensen, Non-Hermitian Sonic Second-Order Topological Insulator, *Phys. Rev. Lett.* **122**, 195501 (2019).
- [60] Z. Zhang, H. Long, C. Liu, C. Shao, Y. Cheng, X. Liu, and J. Christensen, Deep-subwavelength holey acoustic second-order topological insulators, *Adv. Mater.* **31**, 1904682 (2019).
- [61] F. Liu, H.-Y. Deng, and K. Wakabayashi, Helical Topological Edge States in a Quadrupole Phase, *Phys. Rev. Lett.* **122**, 086804 (2019).
- [62] Z. Zhang, B. Hu, F. Liu, Y. Cheng, X. Liu, and J. Christensen, Pseudospin induced topological corner state at intersecting sonic lattices, *Phys. Rev. B* **101**, 220102(R) (2020).
- [63] B. Xie, G. Su, H.-F. Wang, F. Liu, L. Hu, S.-Y. Yu, P. Zhan, M.-H. Lu, Z. Wang, and Y.-F. Chen, Higher-order quantum spin Hall effect in a photonic crystal, *Nat. Commun.* **11**, 3768 (2020).